



HAL
open science

Experimental and numerical study of laser-induced secondary jetting

R T Cerbus, H Chraibi, M Tondusson, S Petit, D Soto, R Devillard, J P Delville, Hamid Kellay

► **To cite this version:**

R T Cerbus, H Chraibi, M Tondusson, S Petit, D Soto, et al.. Experimental and numerical study of laser-induced secondary jetting. *Journal of Fluid Mechanics*, 2022, 934, pp.A14. 10.1017/jfm.2021.1117. hal-03526392

HAL Id: hal-03526392

<https://cnrs.hal.science/hal-03526392v1>

Submitted on 14 Jan 2022

HAL is a multi-disciplinary open access archive for the deposit and dissemination of scientific research documents, whether they are published or not. The documents may come from teaching and research institutions in France or abroad, or from public or private research centers.

L'archive ouverte pluridisciplinaire **HAL**, est destinée au dépôt et à la diffusion de documents scientifiques de niveau recherche, publiés ou non, émanant des établissements d'enseignement et de recherche français ou étrangers, des laboratoires publics ou privés.

Experimental and numerical study of laser-induced secondary jetting

R. T. Cerbus¹, H. Chraïbi¹, M Tondusson¹, S. Petit², D. Soto⁴, R. Devillard³, J. P. Delville¹, and H. Kellay¹†

¹Université Bordeaux- CNRS, LOMA, UMR 5798, F33405 Talence, France

²Université Bordeaux- CNRS- CEA, CELIA, UMR 5107, F33405 Talence, France

³Université Bordeaux, INSERM, BIOTIS, UMR1026, F-33000, Bordeaux France

⁴Poetis, Bioparc Bordeaux Métropole - Bat C 27 allée Charles Darwin, 33600 Pessac

(Received xx; revised xx; accepted xx)

The generation of liquid jets and drops using tightly focused femtosecond laser pulses near a liquid-air interface is a convenient contactless solution for printing functional materials as well as bio-materials. Jets and drops emerge following the nucleation of a cavitation bubble in the liquid bulk by a laser-induced plasma. During the initial expansion of the bubble, a thin and fast jet is produced at the liquid surface. Moments later a second thick and slow jet emanates from the surface when the bubble has nearly deflated. Despite potential applications, little is known about the mechanism behind this complex phenomenology. Here experiments and simulations are used to investigate this two-jet process. Counter-intuitively, the second jet is not the result of bubble expansion, as with the first jet, but originates from the secondary flows induced by the bubble dynamics. Our study links the second jet properties to the control parameters of the problem and establishes a phase diagram for its emergence.

1. Introduction

Printing functional materials for organic electronics applications or biological inks in tissue engineering is an intricate challenge as the printing techniques must often be adapted to the material properties. These properties can be complex, with fluids ranging from Newtonian to viscoplastic and viscoelastic. Many printing techniques rely on physical contact between the ink and a blade, a nozzle, or a pattern (Yan *et al.* 2018; Zhou *et al.* 2020; Glasser *et al.* 2019; Deblais *et al.* 2016). Contact between the fluid and the solid surfaces of the printing device can cause clogging or degradation of the material through substantial shear or extension. These modifications can be desirable for certain printing techniques. Shear thinning is useful for inkjet printing and the presence of a yield stress is useful for blade coating. Nevertheless, the high sensitivity of printing processes to both fluid and mechanical properties narrows the utility of each method. A robust and flexible technique which avoids such drawbacks is Laser Induced Forward Transfer (LIFT) (Bohandy *et al.* 1986). A submerged bubble is nucleated near a liquid-gas interface by a laser-induced plasma, whose subsequent dynamics produces liquid jets accomplishing material transportation and deposition. As it is contactless and nozzle free, LIFT can be adapted to different materials from Newtonian or complex liquids to biological materials for printing, dispensing controlled amounts of fluid, or producing jets with very high velocities intended for hypodermic injections (Desrus *et al.* 2016; Petit *et al.* 2017; Brown *et al.* 2012; Yan *et al.* 2012; Zhang *et al.* 2015; Jalaal *et al.* 2019b;

† Email address for correspondence: hamid.kellay@u-bordeaux.fr

Turkoz *et al.* 2017, 2018; Mézel *et al.* 2010; Ali *et al.* 2014; Gruene *et al.* 2011; Tagawa *et al.* 2012). This technique is used in two configurations. The first configuration requires the presence of a sacrificial film, such as a metallic film, which is heated (and damaged) by the laser light to produce an expanding bubble and eventually liquid jets (Brown *et al.* 2012; Yan *et al.* 2012; Zhang *et al.* 2015; Turkoz *et al.* 2017, 2018; Ali *et al.* 2014; Gruene *et al.* 2011). In the second configuration, investigated here, the laser is focused directly in the bulk of a fluid layer just beneath the liquid-air interface (Desrus *et al.* 2016; Petit *et al.* 2017; Patrascioiu *et al.* 2014*b*; Jalaal *et al.* 2019*b*). This configuration is attractive for applications including bio-printing as it minimizes the presence of impurities engendered by the eventual degradation of a sacrificial film.

An obstacle of both LIFT configurations is the complex phenomenology of the jet formation, with most reports showing that this occurs in two stages (Petit *et al.* 2017; Patrascioiu *et al.* 2014*b*; Jalaal *et al.* 2019*b*). The first stage produces very thin ($\sim 10 \mu\text{m}$) and fast ($\sim 10 \text{ m/s}$) jets. In the second stage, a relatively thick ($\sim 100 \mu\text{m}$) and slow ($\sim 1 \text{ m/s}$) jet is produced. The first jet can be utilised for high resolution printing if the comparatively thicker second jet is avoided. However, the first jet is too thin to be suitable for printing functional materials such as suspensions of large particles or bio-materials such as cells, which the second jet is potentially capable of. If properly understood, this complexity can be exploited to provide a versatile printing method.

The fluid mechanics of the interaction between an oscillating bubble and a free surface have been studied for some time (Lauterborn & Kurz 2010; Pearson *et al.* 2004), with military applications of underwater explosions providing an early motivation to understand this phenomena (Davies & Taylor 1942). Observations and analysis of principally the first jet in laboratory-scale experiments have steadily provided new insights into the bubble dynamics and first jet formation, aided by improved technology and numerical simulations (Chahine 1977; Chahine & Bovis 1980; Blake & Gibson 1987; Robinson *et al.* 2001; Patrascioiu *et al.* 2014*b*). There appears to be broad consensus that the first jet is engendered by the impulse of the initial expansion of the bubble after initiation (Patrascioiu *et al.* 2014*a*). In particular, there is good overall agreement between experiments and theoretical calculations which employ the Kelvin impulse (Blake & Gibson 1987). And more recent analysis using a boundary integral formulation can quantitatively reproduce the detailed features of the first jet and even its counter-jet (Pearson *et al.* 2004). The dynamics of and mechanism behind the second jet formation, on the other hand, is comparatively less studied and understood.

Although the second jet itself has not been as extensively studied, there are numerous studies that, while focusing on the first jet, also investigated the formation of a crown that can follow the emergence of the first jet (Li *et al.* 2019; Liu *et al.* 2017; Koukouvinis *et al.* 2016; Kiyama *et al.* 2016). The formation of the crown and the formation of the second jet appear to be intricately linked. Although some have argued that compressibility effects such as large pressure waves are responsible for the crown (Kiyama *et al.* 2016), explicitly incompressible simulations (Liu *et al.* 2017) that reproduce the crown demonstrate that compressibility is not essential to the phenomenon. Moreover the effects of the shock produced by the bubble nucleation last for only a few microseconds after bubble nucleation (Jalaal *et al.* 2019*a*), well before the formation of the second jet, and a recent parametric study of the crown formation concluded that the shock wave impinging on the surface is not responsible for the crown (Saade *et al.* 2021).

Here, by carrying out a comprehensive experimental and numerical study, we clarify the mechanism behind the formation of the second jet and elucidate both its properties and the conditions for its emergence. We demonstrate that the mechanism behind the second jet formation is unique and unlike the mechanism behind the first jet formation.

In particular, the origin of the second jet is the secondary flow generated by the bubble dynamics. The paper is organized as follows. In §2, we provide information regarding the experimental setup and the numerical methods. In §3, we present our initial experimental and numerical results, showing the broad agreement between these two approaches. In §4 we elucidate the mechanism behind the formation of the second jet and use this to formulate a scaling argument to understand the dependence of the second jet velocity on parameters such as initial bubble depth and pressure. Finally, in §5 we summarize our findings.

2. Experimental and numerical methods

Our experimental setup consists of an amplified Titane Sapphire Femtosecond Laser emitting at 800 nm with a pulse duration of 65 fs, pulse energy of 3 mJ, and a repetition rate of 1kHz. A Pockels cell, synchronised with the laser, selects a smaller repetition rate going from a fraction of a Hz to several Hz. The laser beam, of typical radius 2mm, is then focused with a long working distance microscope objective (50x N.A. 0.5 (Olympus SLMPLN series)) in a volume of liquid (ultrapure water from a Millipore/Milli Q system) contained in a rectangular fused quartz cell (Hellma 101.150 ϕ s) with a square transparent base of 1 cm². The pulse energy can be varied using a half-wave plate combined with a polarizing beamsplitter from 2.5 to 30 μ J. The objective was mounted on a stage for a precise positioning of the focal point with respect to the liquid-air interface. The Laser beam waist was estimated to be roughly 1 micron. The cell walls were rendered hydrophobic using OTS (octadecyltrisiloxane) in Toluene solution to minimize the effect of the meniscus on the visualization. A high speed camera (Phantom V 640) equipped with a magnifying lens (Navitar) was then used to visualize the dynamics of both bubble and jet formation. Typical frame rates were 110000 frames/s with an exposure time of 1 μ s. The spatial resolution was 3.5 μ m/pix. The acquisition of the images from the camera was triggered using a train of pulses delivered by an Agilent generator, itself synchronized to a recurring starting pulse powered by the Pockels cell driver.

For the numerical simulations, we use the open-source package OPENFOAM (Jasak *et al.* 2007), a finite-volume solver for partial differential equations such as the Navier-Stokes equations. For the time integration we use an Euler scheme with the time step dynamically set to ensure a maximum Courant number less than 0.25. We use *compressibleInterFOAM*, a solver for two compressible, non-isothermal immiscible fluids, which uses a volume of fluid (VoF) method to solve for the volume fraction of the liquid phase γ with the transport equation (Miller *et al.* 2013; Koch *et al.* 2016; Zeng *et al.* 2020)

$$\frac{\partial \gamma}{\partial t} + \nabla \cdot (\gamma \mathbf{u}) + \nabla \cdot (\gamma(1 - \gamma) \mathbf{U}_r) = \gamma(1 - \gamma) \left(\frac{1}{\rho_g} \frac{D\rho_g}{Dp_g} - \frac{1}{\rho_l} \frac{D\rho_l}{Dp_l} \right) \frac{Dp}{Dt} + \gamma \nabla \cdot \mathbf{u}, \quad (2.1)$$

where \mathbf{u} is the velocity field, t is time, p is the pressure, ρ is the density, and the subscripts g and l represent the gas and liquid phases respectively. The final term on the left hand side is an artificial term that counteracts the numerical diffusion of the interface keeping it sharp (Koch *et al.* 2016; Rusche 2003). The compressibilities $D\rho/Dp$ are determined by the equation of state for the gas and liquid phases, which for simplicity we choose to be the ideal gas and fluid laws, neglecting higher-order effects of temperature and pressure (Miller *et al.* 2013; Koch *et al.* 2016). Numerical simulations using *compressibleInterFOAM* have recently been performed to study cavitation and jetting in thin gaps (Zeng *et al.* 2020).

Heat and mass transfer are neglected, and the governing equations for the motion of

the fluid are then the continuity equation

$$\frac{\partial \rho}{\partial t} + \nabla \cdot (\rho \mathbf{u}) = 0, \quad (2.2)$$

and the compressible Navier-Stokes equations

$$\frac{\partial \rho \mathbf{u}}{\partial t} + \nabla \cdot (\rho \mathbf{u} \mathbf{u}) = -\nabla p + \nabla \cdot \boldsymbol{\tau} + \mathbf{F}, \quad (2.3)$$

where $\boldsymbol{\tau}$ is the viscous stress tensor $\boldsymbol{\tau} = \mu[\nabla \mathbf{u} + \nabla \mathbf{u}^T - \frac{2}{3}(\nabla \cdot \mathbf{u})\mathbf{I}]$, with μ the dynamic viscosity and \mathbf{I} the identity tensor. \mathbf{F} is the force due to surface tension which is modelled using a continuous-surface-force method which preserves the sharpness of the interface in order to accurately estimate the curvature (Koch *et al.* 2016; Brackbill *et al.* 1992).

Eqs. 2.1-2.3 are solved together in a rectilinear domain. The extent of the three-dimensional (3D) simulation domain was 400 μm in both horizontal directions (x , y) and ranged from 800 μm to 1200 μm in the vertical direction (z), with the liquid-air interface ($z = 0$) fixed at 300 μm above the domain bottom. We used a uniform resolution of $dx = 2 \mu\text{m}$. The boundary conditions are zero-gradient at all domain boundaries. More information on the sensitivity to domain size and resolution can be found in App. A.

Simulating the exact experimental situation, including the laser-fluid interaction, is complex. To simplify our approach, we assume that this interaction simply nucleates a small bubble of initial high pressure P beneath the surface at $z = -H$ ($x = y = 0$). We use a spherical bubble with initial radius $R_0 = 10 \mu\text{m}$, which remains roughly spherical during the initial dynamics. This is significantly different from experiments where the bubbles observed experimentally are elongated in the direction of the beam (the focal area is a vertically elongated ellipsoid due to the necessarily weak numerical aperture of the long working distance objective). As we show, despite these simplifications, our numerical simulations capture the essential features of the experimental observations.

3. Results

In experiments we vary both the focal point depth H below the interface as well as the pulse energy E . The typical phenomenology of the jet formation following bubble nucleation for a fixed E and $H = 144 \mu\text{m}$ is shown in Fig. 1. After nucleation, the bubble rapidly expands, reaches a maximum size, then contracts and recoils away from the interface. Notwithstanding the presence of the interface and substantial asymmetry, the bubble dynamics is in fair agreement with the predicted behavior of the Rayleigh-Plesset equation (Vogel *et al.* 1999; Lauterborn & Kurz 2010) (see App. B). The initial bubble expansion correlates with the formation of the first rapid jet. As this thin jet rises, the bubble deflates and recoils into the bulk fluid. Moments later ($t \sim 30 \mu\text{s}$) a second bulge emerges from the interface and the slower, thicker second jet emerges as in previous observations (Patrascioiu *et al.* 2014b). During the emergence of this second jet the bubble has deflated completely as it recoils away from the interface. While the first jet disintegrates into a train of rapidly rising drops (of size $\sim 20 \mu\text{m}$) the second jet becomes unstable at the tip and engenders drops of much larger size ($D \sim 100 \mu\text{m}$).

The first jet, now well understood, is produced by the impulse of the initial bubble expansion. Previous work has suggested that the mechanism for the second jet is the same (Patrascioiu *et al.* 2014b), with the second jet corresponding to the second bubble expansion. To investigate this in more detail, we have carried out a numerical study which provides information not available in experiments and reveals the detailed velocity and pressure fields responsible for the second jet formation. As with experiments, we

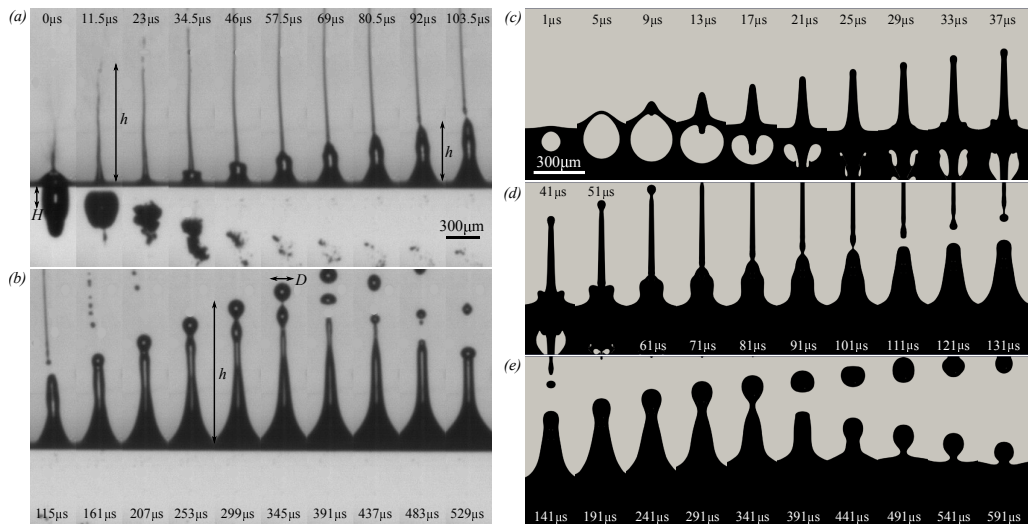


FIGURE 1. (a)-(b) Sequence of side-view images illustrating the experimental bubble and jet dynamics, the nucleation depth H , the jet height h and the droplet diameter D . The laser pulse energy is $E = 18.3 \mu\text{J}$ and $H = 144 \mu\text{m}$. The first thin jet appears concomitantly with the bubble expansion while the second jet emerges $\sim 30 \mu\text{s}$ later when the bubble has deflated and recoiled away from the interface. (c)-(e) Numerical analog of the experimental images. Vertical slices ($y-z$ plane) of the 3D numerical simulations of the bubble and jet dynamics. Here $H = 80 \mu\text{m}$ and the initial bubble pressure is $P = 600$ bars. The second jet is beginning to emerge $\sim 30 \mu\text{s}$ after initiation. The simulations reproduce the main features of the experiments and show additional details such as the counter-jet ($t = 17 \mu\text{s}$) not easily observed in our experiments.

systematically vary H and P , which replaces E , to uncover their significance for the jet's behavior.

To estimate appropriate values of P to correspond with experiments is not a simple task as only a fraction of the pulse energy is transformed into bubble energy (Vogel *et al.* 1999). Following Fabbro *et al.* (1990) and Jalaal *et al.* (2019b), a characteristic pressure due to the laser pulse can be estimated using

$$P_c = (\alpha(I - I_{th}))^{1/2}(\rho c)^{1/2}, \quad (3.1)$$

where I is the laser intensity, I_{th} is the plasma threshold intensity, $\rho = 1000 \text{ kg/m}^3$ is the density of water, and $c = 1500 \text{ m/s}$ is the speed of sound in water, and α ($\simeq 0.01$) is the small fraction of the laser energy that finally contributes to the bubble energy (Vogel *et al.* 1999). With an estimated laser spot radius of $\sim 1 \mu\text{m}$, an energy of $E \sim 1 \mu\text{J}$, and a plasma threshold of $I_{th} \simeq 6 \times 10^{16} \text{ W/m}^2$ (Linz *et al.* 2016), we estimate a characteristic pressure of $P_c \sim 3 \times 10^6$ bars, which although large is of a similar order of magnitude to estimates in similar experiments (Schaffer *et al.* 2002). We confirm this estimate by comparing the oscillations of a bubble nucleated far from the interface with the predictions of the Rayleigh-Plesset equation (see App. B). This comparison suggests a similar order of magnitude for the pressure for an initial bubble radius $R_0 \sim 1 \mu\text{m}$, a scale too small to resolve in our finite spatial resolution simulations. An important parameter, as we will see below, is the bubble energy $\sim PR_0^3$. Keeping this constant we thus increase the initial radius to $R_0 = 10 \mu\text{m}$ and explore initial pressures $10^2 \lesssim P \lesssim 10^3$ bars. Fig. 1 shows a sequence of images of the bubble and jetting dynamics from simulations that are remarkably similar to experiments. A first and second jet, droplet formation, and the

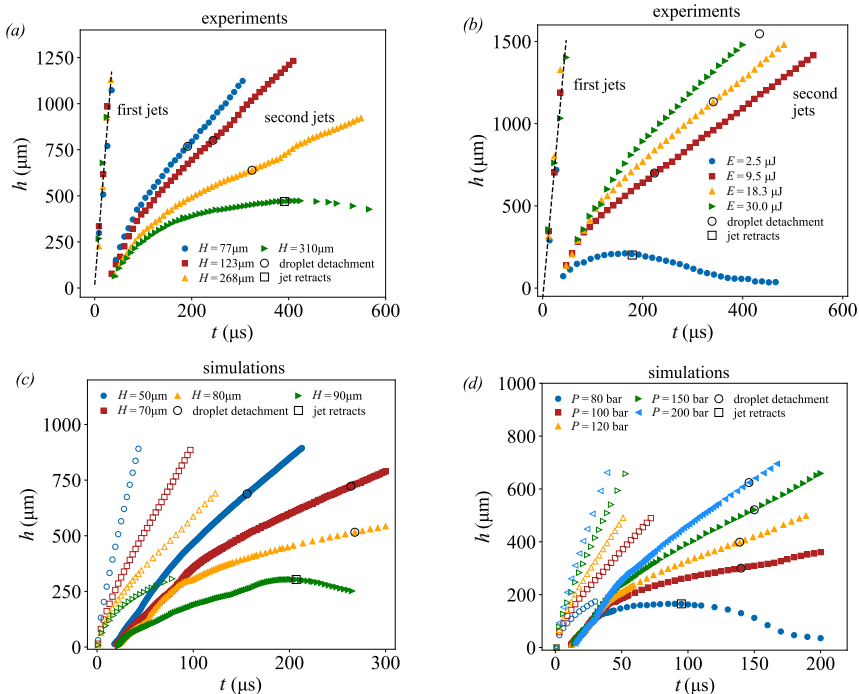


FIGURE 2. (a) Experimental jet height h versus time t for $E = 18.3 \mu\text{J}$ and varying H . For large H no drop formation occurs at the tip of the second jet which simply retracts. (b) Experimental h versus time t for different energies E and $H \approx 120 \mu\text{m}$. (c) h versus time from numerical simulations for different H and fixed initial pressure $P = 400$ bar. The first jet is indicated by open symbols. (d) Same as (c) for different initial pressures P and fixed $H = 40 \mu\text{m}$. The open circles indicate the time at which drop detachment occurs. The data after this time indicate the position of the drop versus time. The drops travels at basically the same velocity as the jet in this regime of roughly constant velocity. The open squares indicate the retraction time.

bubble oscillations are all observed, as well as a counter-jet not easily observable in our experiments (Patrascioiu *et al.* 2014b).

We further compare the experimental and numerical results by studying the dynamics of jet formation for different values of H , E (for experiments), and P (for simulations). In this work we focus on $H \gg R_0$ to avoid bubble bursting (Sanjay *et al.* 2021). In Fig. 2 we plot the heights h of the first and second jets as a function of time, giving a quantitative picture of the phenomenology just described. At early times h corresponds to the jet tip, while at later times it corresponds to the furthest point of the released droplet, if any (see Fig. 1). For experiments, in Fig. 2a we systematically vary H for fixed $E = 18.3 \mu\text{J}$, while in Fig. 2b we systematically vary E for relatively fixed $H \approx 144 \mu\text{m}$. Within our precision the velocity of the first jet U_1 is hardly affected by varying H or E . The velocity U_2 of the second jet, on the other hand, is strongly affected by both H and E . The second jet first decelerates before reaching a steady velocity, U_2 , until it becomes unstable to a Rayleigh-Plateau-like instability engendering droplets with velocities close to that of the rising jet. The open circles in Figs. 2a,2b indicate the position of drop formation. For fixed $E = 18.3 \mu\text{J}$ (Fig. 2a) U_2 is a decreasing function of H until a threshold value of $H = H_c \approx 300 \mu\text{m}$, below which the jet retracts and no droplets are shed. Likewise for a fixed value of $H \approx 144 \mu\text{m}$ (Fig. 2b U_2 shows a systematic dependence on E with a threshold below which no jets can be produced (Vogel *et al.* 1999). The diameter D of the

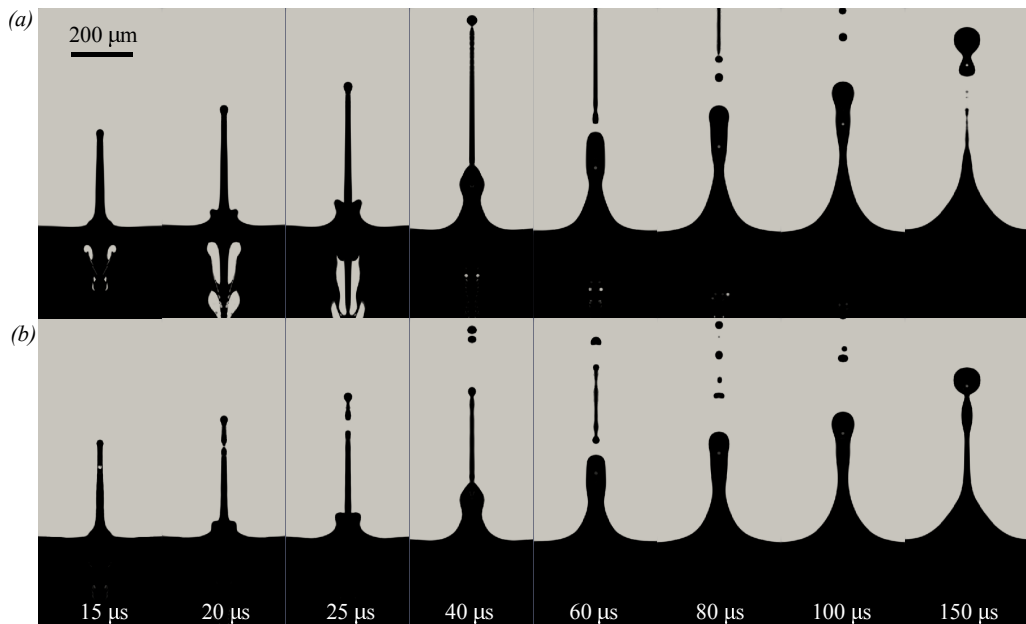


FIGURE 3. Vertical slices of the simulations at different times for $P = 200$ bars and $H = 40 \mu\text{m}$. The liquid (water) phase is dark and the gas (air) phase is light. Until time $t \simeq 14 \mu\text{s}$, when the bubble size reaches its first minimum, the two simulations (a) and (b) are the same with dynamics as in Fig. 1 for $t \lesssim 25 \mu\text{s}$. Then for (b), the bubble is artificially removed by setting the air phase below the interface to water and the simulation allowed to evolve. In this way the second expansion of the bubble is removed. A comparison of the second jet with (a) and without (b) the second expansion shows that the second jet is much the same in its absence.

shed droplets, however, depends only weakly on H and E (see SFig. 2). The sensitivity of U_2 to H and E suggests that it can be tuned to affect how droplets impact a surface for printing (Zhang *et al.* 2016). In Fig. 2c we show the jet time series for different values of H for fixed $P = 400$ bar, while in Fig. 2d we show the same for different values of P with fixed $H = 40 \mu\text{m}$. The time series from the simulations are both qualitatively and quantitatively similar to the experiments. The second jet emergence time ($\sim 20 \mu\text{s}$), the droplet detachment time ($\sim 200 \mu\text{s}$), and the first jet velocity (~ 30 m/s), and second jet velocity (~ 3 m/s) are all quantitatively similar for simulations and experiments. Likewise, the dependence of second jet velocity U_2 and drop diameter D on H and P mimic the experimental behavior with D being less sensitive than U_2 (see App. C). A notable difference between experiments and simulations is the significant dependence of U_1 on H and P in simulations (see Figs. 2c,2d), although our experiments may simply have insufficient temporal resolution to see a similar dependence.

4. Analysis and discussion

While there exists detailed analysis and theory for the initial jet formation due to the expanding bubble (Blake & Gibson 1987; Robinson *et al.* 2001), there appears to be little understanding of the second, thicker jet. Previous work has argued that the mechanism for the second jet differs little from that of the first jet (Patrascioiu *et al.* 2014b): the secondary bubble expansion pushes the fluid away from the free surface into the air. However, in both experiments and simulations, the second jet emerges when the bubble is imploding and recoiling away from the interface, before it has begun its second

expansion (as in Fig. 1 for $t \lesssim 25\mu\text{s}$ and Fig. 5a). If the second jet were the product of the second bubble expansion, then one would expect a delay even longer than the several μs between the first bubble expansion and first jet (see Fig. 1c) since the bubble is even further from the surface when the second jet emerges. The absence of any delay points to the failure of the argument that the second jet arises from the second expansion.

A qualitative test of the hypothesis of the importance of the secondary expansion for the second jet can be made by artificially removing the bubble when it reaches its minimum size in a simulation (see Fig. 3). When the bubble reaches its minimum size at $t \simeq 14\ \mu\text{s}$, after its implosion, we set the phase in the submerged bubble to water, leaving the velocity, pressure and temperature fields as they are. In this way the second expansion is effectively, albeit artificially, removed. A comparison between a simulation with (Fig. 3a) and without (Fig. 3b) the second expansion shows only minute differences. The second jet still emerges and engenders a large droplet. If the second expansion is not responsible for the second jet, its source must be sought elsewhere.

Here the additional information provided by the simulations becomes essential. In Fig. 4 we show the velocity and pressure fields of a representative simulation where $P = 200$ bar and $H = 40\ \mu\text{m}$. These fields are consistent with the explanation that the first jet is created by the initial bubble expansion pushing the fluid upward, the primary flow. The pressure gradient is directed radially away from the bubble, and the velocity is likewise directed radially outward. During the initial formation of the second jet, however, the velocity and pressure fields are significantly different. The pressure is much larger below the surface than at the surface, and the largest gradient occurs when the bubble is at its minimum size ($t = 14\ \mu\text{s}$). The collapse of the bubble, which becomes toroidal, generates a rapidly retracting counter-jet and a substantial inflow into the region between the bubble and the surface ($t = 13\ \mu\text{s}$). This creates the high-pressure region below the surface as well as a saddle flow ($t = 14\ \mu\text{s}$). The lateral flow into the region between the bubble and the surface, which we term the secondary flow and which is established before the bubble expansion, appears to be the source of the second jet. Less than $1\ \mu\text{s}$ later, the second jet has already emerged, well before the bubble re-expands. In Fig. 5a we show the time of the second jet emergence T_{jet} vs. the time that the bubble collapses to its minimum size T_{min} . The near perfect correlation between the two times for all pressures, energies, and depths reinforces our argument that the second jet is related to the bubble contraction, and the secondary flow it engenders, and not the bubble re-expansion. Identifying the secondary flow as the mechanism behind the second jet formation, as done qualitatively in Chen *et al.* (2013), permits a simple analysis of the second jet velocity scaling.

Mass conservation determines a relationship between the secondary inflow velocity and the second jet velocity, U_2 . Although the degree of contribution to the secondary flow from the bubble collapse and counter-jet is unclear, we attribute the large downward flow in Fig. 4a ($t \geq 13\ \mu\text{s}$) to the counter-jet, which we assume has a velocity comparable to the first jet U_1 . By considering a cylindrical volume of liquid of diameter D_c and length l_c , we can write $2\pi(D_c/2)l_cU \sim \pi(D_c/2)^2U_1$, which yields

$$U \sim U_1 \frac{D_c}{4l_c}. \quad (4.1)$$

We anticipate that D_c corresponds to the maximum nucleated bubble size D_{max} while the vertical length scale l_c is as yet unknown. (Additional evidence for a single horizontal length scale proportional to D_{max} is given in Fig. 6a, where we show that the droplet diameter $D \propto D_{\text{max}}$). In Fig. 5b we plot both U_1 and U_2 versus H for simulations at $P = 400$ bar. Both velocities decrease approximately linearly with H and approach zero at $H \sim 90\ \mu\text{m}$, beyond which no jetting is observed. The ratio between U_2 and U_1 is thus

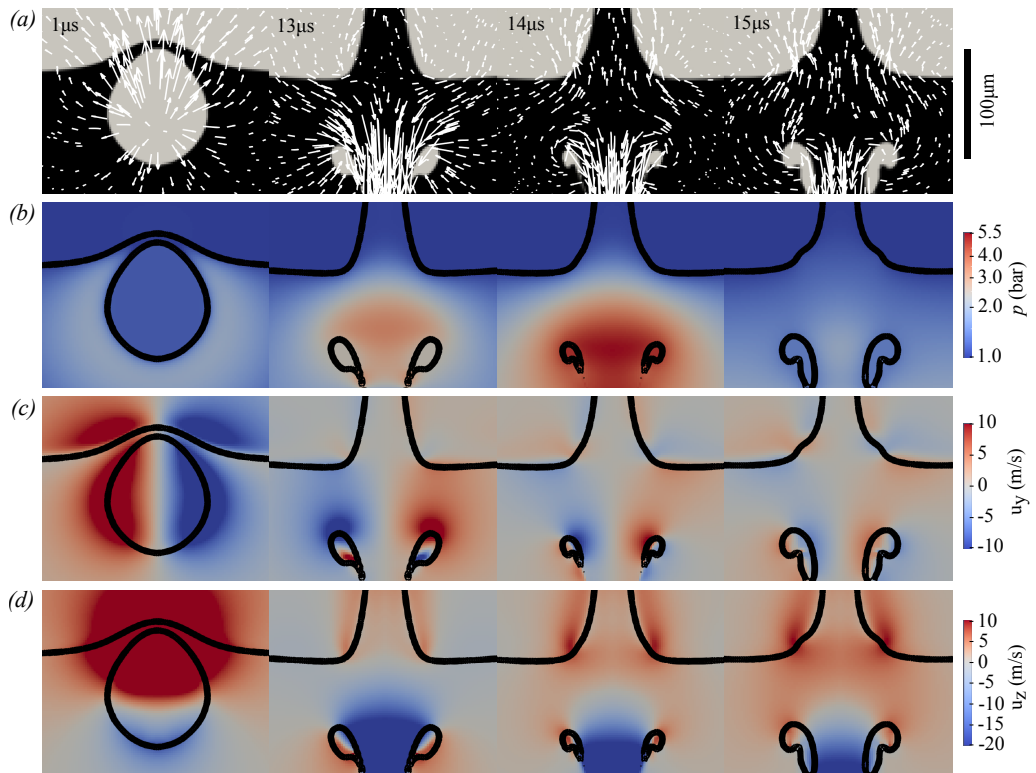


FIGURE 4. Vertical slices of the simulated flow fields at $t = 1, 13, 14,$ and $15 \mu\text{s}$ for $P = 200$ bars and $H = 40 \mu\text{m}$, focusing on the region near the interface. (a) Plots of the liquid (dark) and air (light) phases with velocity vectors super-imposed. The velocity vector lengths at $t = 1 \mu\text{s}$ correspond to the distance a fluid particle will travel in $1 \mu\text{s}$, while the velocity vector lengths for the remaining times correspond to the distance a fluid particle will travel in $2 \mu\text{s}$. (b) Color plots of the pressure field p . The phase boundaries are indicated by thick black lines. (c) Color plots of the horizontal velocity u_y . (d) Color plots of the vertical velocity u_z . The first column ($t = 1 \mu\text{s}$) shows the bubble several μs prior to the emergence of the first jet. The remaining columns are before ($t = 13 \mu\text{s}$), during ($t = 14 \mu\text{s}$), and after ($t = 15 \mu\text{s}$), the emergence of the second jet, which is accompanied by a substantial secondary flow. A substantial secondary flow accompanies the emergence of the second jet, with the flow drawn in by the bubble collapse and counter-jet feeding the second jet and creating the large pressure gradient that drives it.

constant and given by $D_{\max}/4l_c$ (Eq. 4.1), which after measuring D_{\max} yields l_c . In Fig. 6b we show that $l_c \simeq D_{\max}$ for several values of P . The bubble dimensions thus set the relation between U_2 and U_1 .

In Figs. 7a,7b we show that the linearity of U_2 with H up to a threshold value H_c , as in Fig. 5b, is generic for both experiments with fixed E and for additional simulations with fixed P . Unsurprisingly, the critical depth H_c increases while the slope $\partial U/\partial H$ decreases with an increase of E or P . The similarities between these graphs suggest that the experimental and numerical results can be brought into correspondence with a suitable normalization. Since we have argued that the second jet is associated with bubble collapse, we estimate a characteristic bubble collapse velocity as $U_\sigma = \sqrt{\sigma/\rho D_{\max}}$, where σ is the surface tension between water and air, and normalize U_2 with U_σ . To account for the dependence on a critical depth H_c , we plot U_2/U_σ versus $(H_c - H)/D_{\max}$, which is similar to but distinct from the standoff distance $2H/D_{\max}$ used in previous work

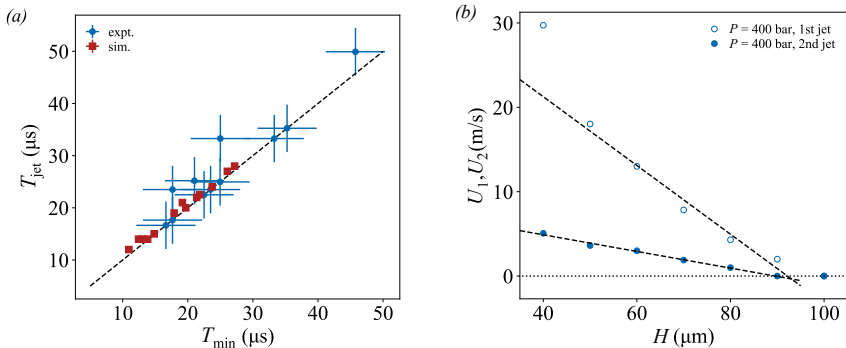


FIGURE 5. (a) Plot of the second jet emergence time T_{jet} vs. the time when the submerged bubble reaches its minimum size T_{min} . The uncertainties on the experimental and numerical results correspond to the time between recorded times, $9 \mu\text{s}$ and $1 \mu\text{s}$ respectively. (b) Plot of the first U_1 and second U_2 jet velocity vs. H for fixed $P = 400$ bar from simulations. Both vary approximately linearly near a threshold value of $H_c \simeq 90 \mu\text{m}$.

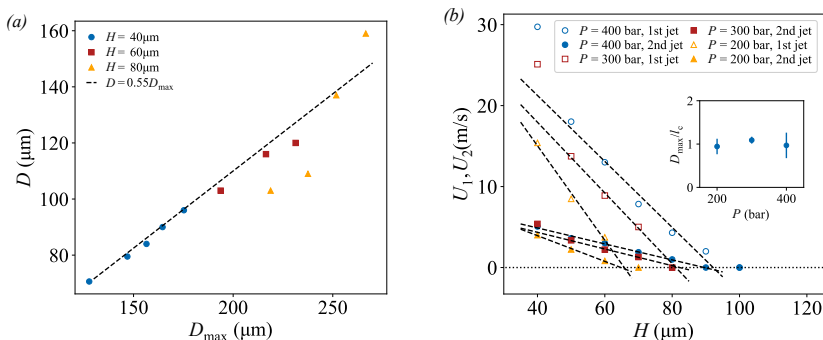


FIGURE 6. (a) Plot of the droplet size D vs. horizontal maximum bubble diameter D_{max}^h from simulations. Combining the results from several depths indicates that $D \propto D_{\text{max}}^h$. (b) Plot of first U_1 and second U_2 jet velocity vs. initial depth H from simulations for three different initial pressures $P = 200, 300$, and 400 bar. For all pressures, both U_1 and U_2 decrease nearly linearly to zero at a critical depth H^* . The ratio of the slopes of these two lines is $D_{\text{max}}^h/4l_c$, as argued in the main text. Inset: D_{max}^h/l_c vs. P . The ratio is close to unity for all P , suggesting that there is only a single dominant length scale.

(Pearson *et al.* 2004) by virtue of the inclusion of H_c necessary for collapse. As Fig. 7c shows, the data collapse satisfactorily. Although the bubbles in the simulations are roughly spherical, the bubbles in experiments are strongly elliptical, so to account for this asymmetry we used the maximum bubble horizontal width D_{max}^h and vertical length D_{max}^v as the relevant length scales. In the simulations these two length scales are nearly the same. If different, as in experiments, we expect the vertical length scale D_{max}^v to affect the critical depth H_c , while we expect the horizontal length D_{max}^h to control the bubble collapse speed. Thus D_{max}^v is used to normalize $(H_c - H)$ and D_{max}^h is used to normalize the velocity. With these choices the experiments and simulations collapse, but separately. To bring them into accord with each other, we introduce a parameter $\beta \simeq 0.48$ which is used only for the simulations to artificially modify the length scales D_{max}^v and D_{max}^h . Since the value of β is close to the ratio of the $D_{\text{max}}^h/D_{\text{max}}^v$ for experiments (see App. B), this suggests that we have fully captured the behavior of both simulations and experiments with the normalization in Fig. 7c, excepting a dependence on the bubble asymmetry at its maximum size.

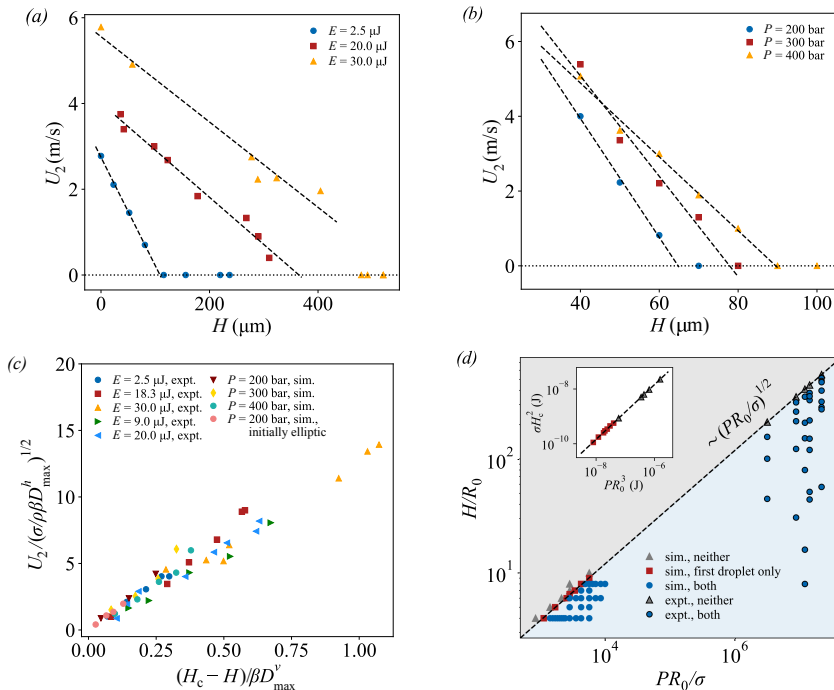


FIGURE 7. The second jet velocity U_2 versus initial depth H for (a) experiments with several fixed E and (b) simulations with several fixed P . All curves reveal the same linearity of U_2 with H and a threshold H_c . (c) Second jet velocity U_2 from experiments and simulations normalized by $U_\sigma = (\sigma/\rho\beta D_{\text{max}}^h)^{1/2}$ versus a normalized distance from the interface $(H_c - H)/\beta D_{\text{max}}^v$. Here $\beta = 0.48$ (close to the experimental ratio $D_{\text{max}}^h/D_{\text{max}}^v \simeq 0.41$) brings the experiments into accord with the simulations, including initially simulations where the initial bubble shape was elliptic (see App. D). (d) Phase diagram for jetting using the two normalized control parameters H/R_0 and PR_0/σ . The interface between jetting and no-jetting scales as $H/R_0 \propto (PR_0/\sigma)^{1/2}$. Inset: Plot of σH_c^2 versus PR_0^3 with the same symbols as the main figure. A linear calibration fit to the simulations determines PR_0^3 for experiments, with P from Eq. 3.1 then yielding R_0 .

We add further evidence to the correspondence between experiments and simulations with a combined phase diagram in Fig. 7d indicating the parameter ranges for jetting and no-jetting. For the simulations we systematically varied H and P to determine when jetting was observed, yielding a jetting to no-jetting boundary empirically found to be $H/R_0 \sim (PR_0/\sigma)^{1/2}$. The scaling of the boundary can be understood by recasting the dependence as $\sigma H_c^2 \sim PR_0^3$, a relationship born out in the inset of Fig. 7d. This simply states that for jetting to occur, the bubble energy must overcome a surface energy (Pearson *et al.* 2004; Chen *et al.* 2013). We note that the length scale of the surface energy H_c is itself simply related to the nucleated bubble dimensions at maximum expansion (see Fig. 10d). The surface in question is thus that which will protrude from the initially flat surface due to a bubble of size $D_{\text{max}} \propto H_c$, with a curvature also set by these length scales. To include the experimental data in the phase diagram requires knowledge of P and R_0 , which we are not able to measure directly. Using a line calibrated to the simulation data in the inset of Fig. 7d, we determine the value of PR_0^3 corresponding to the value of σH_c^2 , which we can determine experimentally. Using P estimated with Eq. 3.1, the value of R_0 turns out to be similar to the beam waist, $\sim 1 \mu\text{m}$, as found in Schaffer *et al.* (2002). The experimental data can then be brought into correspondence with the numerical data in a satisfactory manner as shown in Fig. 7d. Taken together,

Figs. 7c and 7d provide a comprehensive understanding of the jet formation using LIFT as well as the correspondence between laser pulse energy and the engendered pressure giving rise to the cavitation bubble.

5. Conclusion

LIFT near a liquid-air interface results in a complex interaction between the dynamics of a cavitation bubble created by the laser-induced plasma and the shape of the interface. The fast expansion and subsequent implosion of this bubble near the interface generate an initial rapid jet as well as strong secondary flows which give rise to a second more prominent jet. The properties of this jet can be tuned by varying either the focus position of the laser beam with respect to the surface or the incident energy of the laser pulse. Our fully three-dimensional numerical simulations qualitatively and quantitatively reproduce the experimental observations. An important result of our combined numerical and experimental study is a phase diagram of nucleated bubble distance from the interface versus pressure which allows to delimit the jetting and no-jetting regimes. We also explicitly link properties of the jets such as their velocity to these two control parameters. Altogether, our study provides a more complete understanding of the secondary jetting phenomenon and thus how they might be controlled for use in different printing processes where the aim is to deposit materials of large dimensions such as cells or colloids.

Acknowledgements. We thank X. Aguerre, P. Lastanet, J. Flecher, D. Attoumani, for help with preliminary experiments and numerical simulations during their internships.

Funding. H.K. acknowledges support from Institut Universitaire de France, and R.T.C. gratefully acknowledges the support of a Marie Skłodowska-Curie Action Individual Fellowship (MSCAIF).

Declaration of interest. The authors report no conflict of interest.

Appendix A. Simulation sensitivity to domain size and resolution

For the simulations we confirmed insensitivity to both lateral domain size and grid resolution by performing simulations at different lateral domain sizes of 300 μm , 400 μm , 600 μm and 800 μm , and at uniform resolutions of $dx = 4 \mu\text{m}$, $dx = 2 \mu\text{m}$, and $dx = 1.33 \mu\text{m}$. We found no significant change for a lateral domain size larger than 400 μm or a resolution smaller than $dx = 2 \mu\text{m}$. In Fig. 8a we show snapshots of simulations at $t = 25 \mu\text{s}$ after initiation. As the jet time series in Fig. 8b confirms, lateral domains widths of 400 μm and a resolution of $dx = 2 \mu\text{m}$ are sufficient to achieve insensitivity to these parameter choices. We thus adopted these values for the simulations.

Appendix B. Rayleigh-Plesset numerical solution

An additional estimate of the initial experimental bubble pressure is obtained by comparing the oscillations of the bubble diameter with the predictions of the Rayleigh-Plesset equation (see Fig. 9) (Lauterborn & Kurz 2010). In this case the bubble was initiated far from the interface to avoid its influence on the dynamics. We solve the Rayleigh-Plesset equation for the radius R including the effects of viscosity and surface tension

$$\rho R \frac{d^2 R}{dt^2} + \frac{3}{2} \rho \left(\frac{dR}{dt} \right)^2 = P \left(\frac{R_0}{R} \right)^{3\kappa} - P_\infty - \frac{4\mu}{R} \frac{dR}{dt} - \frac{2\sigma}{R}, \quad (\text{B1})$$

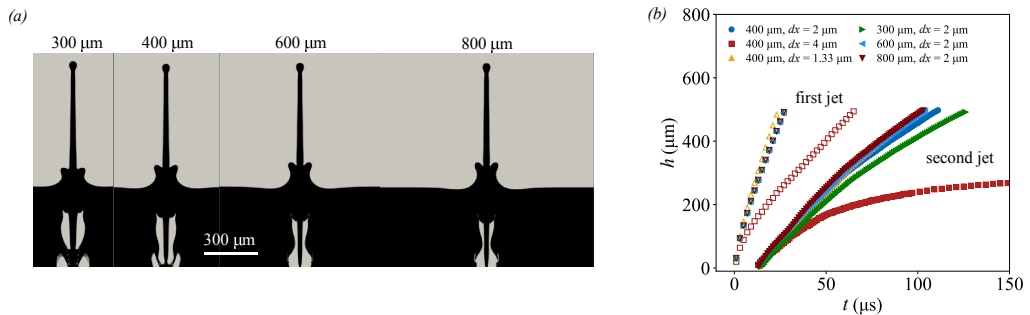


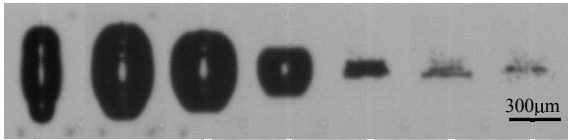
FIGURE 8. (a) Snapshots of simulations (vertical slices) at $t = 25 \mu\text{s}$ after initiation for different domain widths. (b) Time series of first jet (open symbols) and second jet (closed symbols) positions for these same domain widths as well as two different resolutions dx . For domain sizes larger than $300 \mu\text{m}$ and resolutions smaller than $dx = 4 \mu\text{m}$, the results do not differ significantly.

where P and R_0 are the initial pressure and radius of the bubble at rest, $\kappa = 4/3$ is the isentropic expansion factor of water, $P_\infty = 1 \text{ bar}$ is the pressure at infinity, $\mu = 8.9 \times 10^{-4} \text{ kg/m}\cdot\text{s}$ is the dynamic viscosity of water, and $\sigma = 0.072 \text{ N/m}$ is the surface tension between water and air. This equation is integrated forward in time using a fourth order Runge-Kutta method. Because the experimental bubble is axisymmetric, we plot a diameter that accommodates for the cigar shape of the bubble so that we can better compare with the Rayleigh-Plesset theory for symmetric spherical bubbles: $D_{\text{bubble}} = (D_v D_h^2)^{1/3}$, where D_v is the vertical length and D_h is the shorter radial width. We found empirically that at their maximum values $D_h/D_v \simeq 0.41$, which is close to the value of $\beta = 0.48$ used in Fig. 7c. We estimated initial bubble diameters of $R_0 \simeq 1 \mu\text{m}$ in §3 (see Fig. 7d). Assuming that this R_0 corresponds to the smaller horizontal width of the bubble, and using the same ratio of vertical to horizontal length scales found in experiments, the effective initial bubble size used in the numerical solution of the Rayleigh-Plesset equation is then $R_0^* = (R_0^2 (D_v R_0 / D_h))^{1/3} \simeq 1.3 \mu\text{m}$. We find that an estimate of $P = 0.7 \text{ Mbar}$ gives excellent agreement both in terms of spatial and temporal magnitude with the experimental observations, and is close to the estimated value of $P \sim 3 \text{ Mbar}$ found using Eq. 3.1.

Appendix C. Dependence of droplet and bubble diameter

Here we present the droplet and bubble diameter dependence on parameters such as the initial depth H , the initial energy E , or pressure P . The main significance of this presentation is that the droplet diameter D is only weakly dependent on these control parameters, and that the maximum bubble diameter D_{max} is the dominant length scale. In Fig. 10a we show the dependence of the experimental droplet diameter D on the depth H , which follows a weak power law, $D \propto H^{0.225}$. In Fig. 10b we show the dependence of D on the initial energy E , which is also a weak power law, $D \propto E^{0.321}$. We are not aware of any theory that accounts for these power laws. The dependence of the maximum bubble diameter in simulations, D_{max} on pressure P is shown in Fig. 10c. This also follows a weak power-law, $D_{\text{max}} \propto P^{0.383}$ that is consistent with prediction from the Rayleigh-Plesset equation (see App. B). Finally, Fig. 10d shows the dependence of the critical depth H_c on the maximum bubble diameter D_{max} for both simulations and experiments. The dependence is essentially linear, and is in keeping with our finding that D_{max} is the dominant length scale and thus can be used to collapse the plots of velocity versus depth (see Fig. 7c). While in simulations the horizontal and vertical maximum bubble diameters

(a)



(b)

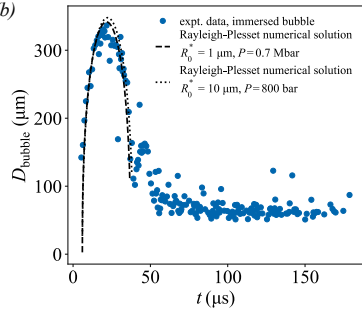


FIGURE 9. (a) Sequence of side-view images illustrating the laser pulse interaction with the liquid. The laser pulse energy is $E = 0.915$ mJ. Here the laser pulse was focused with a 50X magnification microscope objective. Dynamics of a bubble, the black region, nucleated at a large depth ($H = \infty$) far from any interface. The time between images is $9 \mu\text{s}$. The bubble shape is axisymmetric but not spherical, a result of the non-spherical focused laser spot. (b) Plot of immersed bubble diameter D_{bubble} vs. time t from experiments. The laser energy used to initiate this bubble is $E = 18.3 \mu\text{J}$. We also plot the numerical solution when $R_0 = 10 \mu\text{m}$ ($R_0^* \simeq 13.4 \mu\text{m}$), which fits with the experiments when $P = 800$ bar. This result is consistent with $PR_0^3 = \text{const.}$, as argued for Fig. 7d.

are essentially the same, they differ significantly in experiments. That the experiments and simulations should belong to different curves is not surprising, given the differences between them such as initial bubble size and asymmetry. The significance of Fig. 10d is that D_{max} sets the critical depth H_c , just as it also sets the droplet diameter (see Fig. 6a).

Appendix D. Dependence on initial bubble shape

In nearly all of the simulations presented the initial bubble was spherical with radius $R_0 = 10 \mu\text{m}$. In this appendix we present the results of simulations with the same initial volume, and thus the same initial energy PR_0^3 , but with an initially elliptical shape. The ratio of the vertical to horizontal length was 2. Keeping the initial bubble pressure fixed at $P = 200$ bar, we varied the position of the center of the bubble H . Fig. 11a reveals jet time series of the same character as Fig. 2c, with U_1 and U_2 steadily decreasing with increasing H as shown in Fig. 11b. Likewise the plot of U_1 and U_2 vs. H in Fig. 11b is similar to Figs. 5b,7b, with an approximately linear dependence of the asymptotic velocities on H near a critical H_c , although the critical H_c for the first and second jet is slightly different. The normalized velocities are included in Fig. 7c with $\beta \simeq 0.48$ as with the other simulations. The simulations collapse on themselves regardless of the initial bubble shape. Consistent with this, the maximum vertical bubble diameter D_{max}^v differs little from the horizontal diameter D_{max}^h , despite the different initial shape.

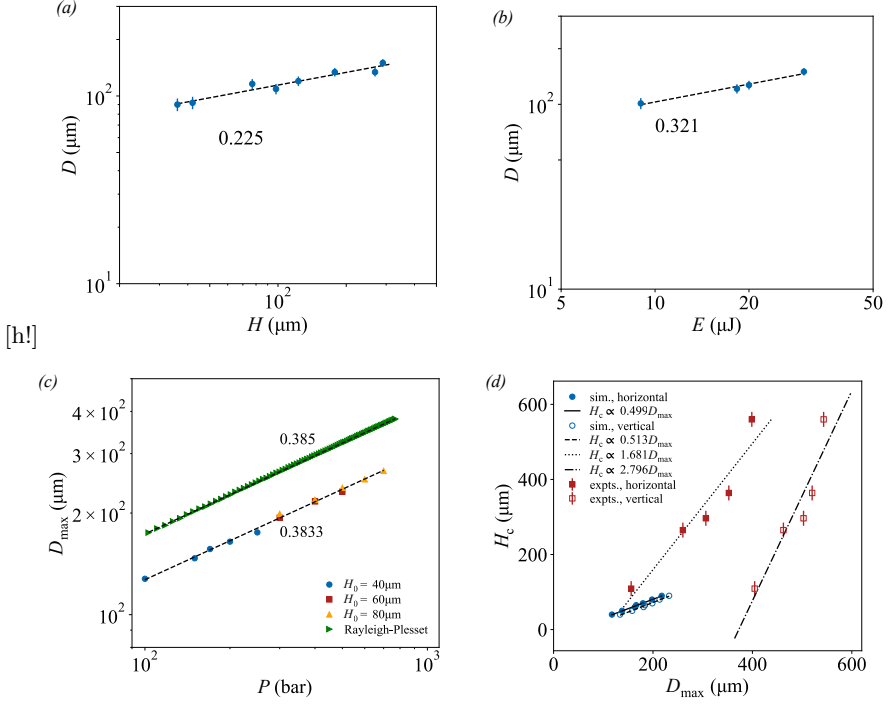


FIGURE 10. (a) Plot of second jet droplet diameter D vs. initial depth H for experiments at fixed energy $E = 18.3\mu\text{J}$. (b) Plot of second jet droplet diameter D vs. energy E for fixed initial depth $H = 125\mu\text{m}$. Unlike the second jet velocity, the droplet diameter D is relatively insensitive to variations in either H or E . (c) Plot of horizontal maximum bubble diameter D_{max}^h vs. initial pressure P for simulations at different depths and the numerical solution of the Rayleigh-Plesset equation. Although the results from simulations are below the prediction of the Rayleigh-Plesset equation, which unlike the simulations assumes the fluid surrounding the bubble extends to infinity in all directions, $D_{\text{max}}^h \propto P^{0.38}$ for both. (d) The empirically-determined critical depths H_c vs. empirically-determined vertical D_{max}^v and horizontal D_{max}^h maximum submerged bubble diameters. While both depend on E or P , H_c and D_{max} are strongly correlated. While for simulations the $D_{\text{max}}^h \simeq D_{\text{max}}^v$, the asymmetry of the initial bubble in experiments results in D_{max}^v being nearly twice as large as D_{max}^h .

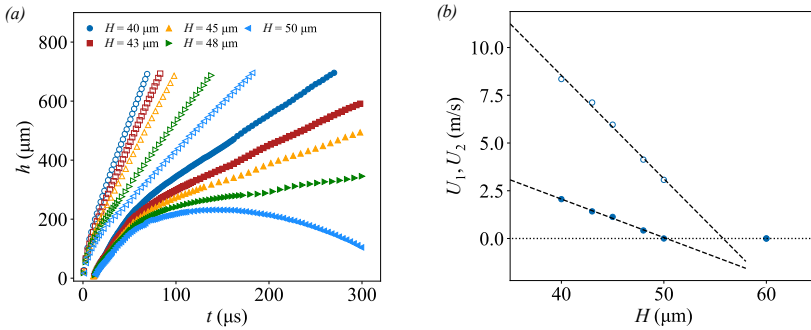


FIGURE 11. (a) Jet height h versus time t for different H and fixed initial pressure $P = 200$ bar for an initially elliptic bubble. The first jet is indicated by open symbols. The same qualitative trends and phenomenology is observed as for simulations with an initially spherical bubble (see Fig. 2c). (b) Plot of the first U_1 and second U_2 jet velocity vs. H for fixed $P = 200$ bar from simulations for an initially elliptic bubble. Both vary approximately linearly near a threshold value of $H_c \simeq 50\mu\text{m}$.

REFERENCES

- ALI, MUHAMMAD, PAGES, EMELINE, DUCOM, ALEXANDRE, FONTAINE, AURELIEN & GUILLEMOT, FABIEN 2014 Controlling laser-induced jet formation for bioprinting mesenchymal stem cells with high viability and high resolution. *Biofabrication* **6** (4), 045001.
- BLAKE, JOHN R & GIBSON, DC 1987 Cavitation bubbles near boundaries. *Annual Review of Fluid Mechanics* **19** (1), 99–123.
- BOHANDY, J, KIM, BF & ADRIAN, FJ 1986 Metal deposition from a supported metal film using an excimer laser. *Journal of Applied Physics* **60** (4), 1538–1539.
- BRACKBILL, JEREMIAH U, KOTHE, DOUGLAS B & ZEMACH, CHARLES 1992 A continuum method for modeling surface tension. *Journal of Computational Physics* **100** (2), 335–354.
- BROWN, MATTHEW S, BRASZ, C FREDERIK, VENTIKOS, YIANNIS & ARNOLD, CRAIG B 2012 Impulsively actuated jets from thin liquid films for high-resolution printing applications. *Journal of Fluid Mechanics* **709**, 341–370.
- CHAHINE, G. L. 1977 Interaction Between an Oscillating Bubble and a Free Surface. *Journal of Fluids Engineering* **99** (4), 709–716.
- CHAHINE, GEORGES L & BOVIS, ALAIN 1980 Oscillation and collapse of a cavitation bubble in the vicinity of a two-liquid interface. In *Cavitation and Inhomogeneities in Underwater Acoustics*, pp. 23–29. Springer.
- CHEN, ROSS CC, YU, YT, SU, KUAN-WEI, CHEN, JENN-FANG & CHEN, YUNG-FU 2013 Exploration of water jet generated by q-switched laser induced water breakdown with different depths beneath a flat free surface. *Optics Express* **21** (1), 445–453.
- DAVIES, RM & TAYLOR, GI 1942 The vertical motion of a spherical bubble and the pressure surrounding it. *The Scientific Papers of GI Taylor* pp. 320–336.
- DEBLAIS, A, HARICH, R, COLIN, A & KELLAY, H 2016 Taming contact line instability for pattern formation. *Nature Communications* **7**, 12458.
- DESRUS, H, CHASSAGNE, B, MOIZAN, F, DEVILLARD, RAPHAËL, PETIT, S, KLING, R & CATROS, SYLVAIN 2016 Effective parameters for film-free femtosecond laser assisted bioprinting. *Applied Optics* **55** (14), 3879–3886.
- FABBRO, R, FOURNIER, J, BALLARD, P, DEVAUX, D & VIRMONT, J 1990 Physical study of laser-produced plasma in confined geometry. *Journal of Applied Physics* **68** (2), 775–784.
- GLASSER, ALIZÉE, CLOUTET, ERIC, HADZIOANNOU, GEORGES & KELLAY, HAMID 2019 Tuning the rheology of conducting polymer inks for various deposition processes. *Chemistry of Materials* **31** (17), 6936–6944.
- GRUENE, MARTIN, UNGER, CLAUDIA, KOCH, LOTHAR, DEIWICK, ANDREA & CHICHKOV, BORIS 2011 Dispensing pico to nanolitre of a natural hydrogel by laser-assisted bioprinting. *Biomedical Engineering Online* **10** (1), 19.
- JALAAL, MAZIYAR, LI, SHUAI, KLEIN SCHAARSBERG, MARTIN, QIN, YIGONG & LOHSE, DETLEF 2019a Destructive mechanisms in laser induced forward transfer. *Applied Physics Letters* **114** (21), 213703.
- JALAAL, MAZIYAR, SCHAARSBERG, MARTIN KLEIN, VISSER, CLAAS-WILLEM & LOHSE, DETLEF 2019b Laser-induced forward transfer of viscoplastic fluids. *Journal of Fluid Mechanics* **880**, 497–513.
- JASAK, HRVOJE, JEMCOV, ALEKSANDAR & TUKOVIC, ZELJKO 2007 Openfoam: A c++ library for complex physics simulations. In *International Workshop on Coupled Methods in Numerical Dynamics*, , vol. 1000, pp. 1–20. IUC Dubrovnik Croatia.
- KIYAMA, AKIHITO, TAGAWA, YOSHIYUKI, ANDO, KEITA & KAMEDA, MASAHARU 2016 Effects of a water hammer and cavitation on jet formation in a test tube. *Journal of Fluid Mechanics* **787**, 224–236.
- KOCH, MAX, LECHNER, CHRISTIANE, REUTER, FABIAN, KÖHLER, KARSTEN, METTIN, ROBERT & LAUTERBORN, WERNER 2016 Numerical modeling of laser generated cavitation bubbles with the finite volume and volume of fluid method, using openfoam. *Computers & Fluids* **126**, 71–90.
- KOUKOUVINIS, PHOEVOS, GAVAISES, MANOLIS, SUPPONEN, OUTI & FARHAT, MOHAMED 2016 Simulation of bubble expansion and collapse in the vicinity of a free surface. *Physics of Fluids* **28** (5), 052103.

- LAUTERBORN, WERNER & KURZ, THOMAS 2010 Physics of bubble oscillations. *Reports on Progress in Physics* **73** (10), 106501.
- LI, TONG, ZHANG, A-MAN, WANG, SHI-PING, LI, SHUAI & LIU, WEN-TAO 2019 Bubble interactions and bursting behaviors near a free surface. *Physics of Fluids* **31** (4), 042104.
- LINZ, NORBERT, FREIDANK, SEBASTIAN, LIANG, XIAO-XUAN & VOGEL, ALFRED 2016 Wavelength dependence of femtosecond laser-induced breakdown in water and implications for laser surgery. *Physical Review B* **94** (2), 024113.
- LIU, NN, CUI, P, REN, SF & ZHANG, AM 2017 Study on the interactions between two identical oscillation bubbles and a free surface in a tank. *Physics of Fluids* **29** (5), 052104.
- MÉZEL, C, SOUQUET, A, HALLO, L & GUILLEMOT, F 2010 Bioprinting by laser-induced forward transfer for tissue engineering applications: jet formation modeling. *Biofabrication* **2** (1), 014103.
- MILLER, ST, JASAK, HRVOJE, BOGER, DA, PATERSON, EG & NEDUNGADI, A 2013 A pressure-based, compressible, two-phase flow finite volume method for underwater explosions. *Computers & Fluids* **87**, 132–143.
- PATRASCIOIU, A, FERNÁNDEZ-PRADAS, JM, MORENZA, JL & SERRA, P 2014a Film-free laser printing: Jetting dynamics analyzed through time-resolved imaging. *Applied Surface Science* **302**, 303–308.
- PATRASCIOIU, A, FERNÁNDEZ-PRADAS, JM, PALLA-PAPAVLU, A, MORENZA, JL & SERRA, P 2014b Laser-generated liquid microjets: correlation between bubble dynamics and liquid ejection. *Microfluidics and Nanofluidics* **16** (1-2), 55–63.
- PEARSON, A, COX, E, BLAKE, JR & OTTO, SR 2004 Bubble interactions near a free surface. *Engineering Analysis with Boundary Elements* **28** (4), 295–313.
- PETIT, STEPHANE, KÉROURÉDAN, OLIVIA, DEVILLARD, RAPHAEL & CORMIER, ERIC 2017 Femtosecond versus picosecond laser pulses for film-free laser bioprinting. *Applied Optics* **56** (31), 8648–8655.
- ROBINSON, PB, BLAKE, JR, KODAMA, T, SHIMA, A & TOMITA, Y 2001 Interaction of cavitation bubbles with a free surface. *Journal of Applied Physics* **89** (12), 8225–8237.
- RUSCHE, HENRIK 2003 Computational fluid dynamics of dispersed two-phase flows at high phase fractions. PhD thesis, Imperial College London (University of London).
- SAADE, YOUSSEF, JALAAL, MAZIYAR, PROSPERETTI, ANDREA & LOHSE, DETLEF 2021 Crown formation from a cavitating bubble close to a free surface. *Journal of Fluid Mechanics* **926**.
- SANJAY, VATSAL, LOHSE, DETLEF & JALAAL, MAZIYAR 2021 Bursting bubble in a viscoplastic medium. *Journal of Fluid Mechanics* **922**, A2.
- SCHAFFER, CHRIS B., NISHIMURA, NOZOMI, GLEZER, ELI N., KIM, ALBERT M.-T. & MAZUR, ERIC 2002 Dynamics of femtosecond laser-induced breakdown in water from femtoseconds to microseconds. *Optics Express* **10** (3), 196–203, publisher: Optical Society of America.
- TAGAWA, YOSHIYUKI, OUDALOV, NIKOLAI, VISSER, CLAAS WILLEM, PETERS, IVO R, VAN DER MEER, DEVARAJ, SUN, CHAO, PROSPERETTI, ANDREA & LOHSE, DETLEF 2012 Highly focused supersonic microjets. *Physical Review X* **2** (3), 031002.
- TURKOZ, EMRE, DEIKE, LUC & ARNOLD, CRAIG B 2017 Comparison of jets from newtonian and non-newtonian fluids induced by blister-actuated laser-induced forward transfer (BALIFT). *Applied Physics A* **123** (10), 652.
- TURKOZ, EMRE, PERAZZO, ANTONIO, KIM, HYOONGSOO, STONE, HOWARD A & ARNOLD, CRAIG B 2018 Impulsively induced jets from viscoelastic films for high-resolution printing. *Physical Review Letters* **120** (7), 074501.
- VOGEL, ALFRED, NOACK, J, NAHEN, K, THEISEN, D, BUSCH, S, PARLITZ, U, HAMMER, DX, NOOJIN, GD, ROCKWELL, BA & BIRNGRUBER, R 1999 Energy balance of optical breakdown in water at nanosecond to femtosecond time scales. *Applied Physics B: Lasers & Optics* **68** (2).
- YAN, JINGYUAN, HUANG, YONG, XU, CHANGXUE & CHRISEY, DOUGLAS B 2012 Effects of fluid properties and laser fluence on jet formation during laser direct writing of glycerol solution. *Journal of Applied Physics* **112** (8), 083105.
- YAN, QIAN, DONG, HANHUA, SU, JIN, HAN, JIANHUA, SONG, BO, WEI, QINGSONG & SHI, YUSHENG 2018 A review of 3d printing technology for medical applications. *Engineering* **4** (5), 729–742.

- ZENG, QINGYUN, GONZALEZ-AVILA, SILVESTRE ROBERTO & OHL, CLAUS-DIETER 2020 Splitting and jetting of cavitation bubbles in thin gaps. *Journal of Fluid Mechanics* **896**.
- ZHANG, ZHENGYI, XIONG, RUITONG, CORR, DAVID T & HUANG, YONG 2016 Study of impingement types and printing quality during laser printing of viscoelastic alginate solutions. *Langmuir* **32** (12), 3004–3014.
- ZHANG, ZHENGYI, XIONG, RUITONG, MEI, RENWEI, HUANG, YONG & CHRISEY, DOUGLAS B 2015 Time-resolved imaging study of jetting dynamics during laser printing of viscoelastic alginate solutions. *Langmuir* **31** (23), 6447–6456.
- ZHOU, LU-YU, FU, JIANZHONG & HE, YONG 2020 A review of 3d printing technologies for soft polymer materials. *Advanced Functional Materials* p. 2000187.